On the room- and elevated-temperature tensile properties of hot-rolled 6082 alloys containing thermally stable dispersoids

E.M. Elgallad*, Z. Chen, X.-G. Chen
Department of Applied Sciences, University of Quebec at Chicoutimi,
Saguenay (QC), Canada G7H 2B1

Abstract

The microstructural evolution and room/elevated-temperature tensile properties of Al-Mg-Si 6082 alloys subjected to thermomechanical processing (homogenization, hot rolling, T6 heat treatment, and thermal exposure) were investigated. Four experimental 6082 alloys were studied, including a Mn-free base alloy and three alloys containing Mn individually and in combination with Cr + V or Mo, in which a number of α-Al(MnFe)Si, α-Al(MnFeCrV)Si and α-Al(MnFeMo)Si dispersoids were formed, respectively. The results showed that both α-Al(MnFeCrV)Si and α-Al(MnFeMo)Si dispersoids had a higher coarsening resistance compared to α-Al(MnFe)Si dispersoids. The presence of α-dispersoids hindered the formation of Mg-Si clusters, which decreased the precipitation of β''-MgSi precipitates, resulting in reductions in room-temperature strengths. During thermal exposure at 300 ºC, the α-dispersoids remained thermally stable and became the predominant strengthening phase, resulting in increases of 71 to 126% in the yield strength at 300 ºC relative to the base alloy without dispersoids. Among the three dispersoid-containing alloys studied, the alloy containing Mn and Mo exhibited the highest yield strength of 70 MPa at 300 ºC, providing the best combination of room- and elevated-temperature tensile properties.

Keywords: Al-Mg-Si 6082 alloy; transition elements; dispersoid strengthening; precipitation hardening; elevated-temperature tensile properties.

*Corresponding author Tel.: +1 418 545 5011 # 2558; Fax: +1 418 545 5012.
E-mail address: emad_elgallad@uqac.ca (E.M. Elgallad)

1. Introduction

Al-Mg-Si 6082 alloys as lightweight and medium- to high-strength materials are widely used in the transportation industries and load-bearing engineering structural applications, such as automobile vehicles, marine crafts, light rails, bridges, cranes, and building structures (Ref 1-3). Such applications may involve high-temperature exposure as thermal-resistant materials and fire-resistant structures (Ref 3-7), which necessitates enhancing the elevated-temperature mechanical properties of these aluminum products. Al-Mg-Si 6082 alloys are heat-treatable wrought alloys and are generally strengthened by the precipitation strengthening of nanoscale β''/β'-MgSi precipitates with T5 and T6 tempers resulting in high room-temperature strengths. However, at high temperatures (> 200 °C) the strength of 6082 alloys dramatically drops owing to the rapid coarsening of MgSi precipitates (Ref 8, 9). In recent years, the demand for high performance and lightweight structural materials at elevated temperatures is highly growing, which is a great challenge for conventional aluminum alloys. Therefore, developing cost effective and high-strength aluminum alloys for various elevated-temperature applications is particularly attractive in different industrial sectors.

Elevated-temperature mechanical properties of aluminum alloys could be improved by adding low-diffusivity transition elements (TEs) (Ref 10). Many efforts have been made to add TEs individually or in combination to aluminum alloys to form suitable thermally stable phases in the Al matrix. Amongst these elements, Mn drew more attention due to its relatively high solubility in α-Al and low price (Ref 8). Different types of thermally stable Mn-bearing dispersoids with various crystallographic structures and chemical compositions were reported to be formed in Al alloys, which included Al_4Mn, Al_6Mn, $Al_6(MnFe)$, and α-$Al_{12}Mn_3Si$/$Al_{12}(MnFe)_3Si$ dispersoids (Ref 11-16). They formed during the heat treatment of the as-cast alloys at temperatures between 350 ºC and 600 ºC through the decomposition of the α-Al solid solution being supersaturated after solidification with Mn, Fe, and Si (Ref 11, 13, 15, 17, 18).

The α-Al(MnFe)Si dispersoids exhibit either simple cubic (SC) or body-centered cubic (BCC) crystal structure (Ref 19). They were mostly precipitated in commercial 3xxx and 6xxx alloys, significantly improving the yield strength and creep resistance at 300 ºC (Ref 13-16), as well as the recrystallization resistance during both hot deformation and post-deformation annealing (Ref 15, 20). The characteristics (size and number density) of these dispersoids could be optimized by using different heat treatments (Ref 8, 13, 15, 21, 22) and stimulating their nucleation (Ref 14, 23). Both one-step 375°C/48h and two-step 250°C/24h + 375°C/48h heat treatments yielded a large number of α-

Al(MnFe)Si dispersoids and consequently peak strengthening at 300 ºC in 3004 alloys (Ref 13, 21). On the other hand, the optimum precipitation of α-Al(MnFe)Si dispersoids occurred in 6082 alloys with low-temperature homogenization at 400 ºC for 2 to 10 h (Ref. 8, 15, 22). Li *et al*. (Ref 14) improved the dispersoid characteristics in 3xxx alloys by optimizing the Si and Mg levels, as these elements affected the precipitation of *β′*-MgSi precipitates during the early stages of heat treatment, which would act as potential nucleation sites for the dispersoids.

The elevated-temperature mechanical behavior of the 3xxx and 6xxx alloys could be further improved by adding other TEs, such as Mo, Cr, and V (Ref 7, 22, 24). These elements have a crystal structure similar to that of Mn and Fe (BCC) with comparable atomic radii but with lower diffusivity; thus, they can substitute for Mn and Fe in the α-Al(MnFe)Si dispersoids, increasing the thermal stability of these dispersoids and consequently the elevated-temperature mechanical properties. Ma *et al*. (Ref 7) demonstrated that micoalloying 3004 alloys with Mo increased the number density and the volume fraction of the dispersoids and decreased the dispersoid-free zones, thereby improving the elevated-temperature tensile properties. Moreover, the Mo-containing dispersoids (α-Al(MnFeMo)Si) showed high coarsening resistance, maintaining high elevated-temperature strength after thermal exposure at 400 °C for 100 h. Elgallad *et al*. (Ref 22) found that 6082 alloys containing Cr, V, and Mo in addition to Mn exhibited improvements in the yield strength at room temperature and 300 °C through the dispersoid refinement, which also contributed to increasing the creep resistance of the alloys at 300 °C.

In our previous study (Ref 22), it is demonstrated that by introducing a large number of α-Al(MnFe)Si/Al(MnFeX)Si dispersoids, where X stands for Cr, V, or Mo, elevated-temperature properties of 6082 alloys were significantly improved. However, the research focused on cast ingots, which did not fully reveal the potential of these alloys as thermal-resistant materials, because the commercial 6082 alloys are generally subjected to thermomechanical processes, such as hot rolling and extrusion. Moreover, the balance between room- and elevated-temperature mechanical properties was not evaluated when combining the dispersoid strengthening with the precipitation hardening. The present study was undertaken to investigate the effects of TEs (Mn, Cr, V, and Mo) on the evolution of both MgSi precipitates and α-dispersoids in 6082 alloys during a typical thermomechanical process involving homogenization, hot rolling, T6 heat treatment, and thermal exposure at 300 ºC. In addition, the room/elevated-temperature tensile properties of rolled sheets of these alloys after T6 heat treatment and thermal exposure at 300 ºC were evaluated.

2. Experimental procedures

Four Al-Mg-Si 6082 alloys with different additions of TEs were used in this study, including the base alloy without TEs, one alloy containing Mn, one alloy having a combination of Mn, Cr, and V, and another alloy with Mn and Mo. The actual chemical compositions of these alloys, analyzed by an optical emission spectroscopy, are listed in Table 1. The melting and casting procedures of the alloys were described in details in the previous study (Ref 22). All alloys were subjected to thermomechanical processing, as illustrated in Fig. 1, in which the cast ingots were homogenized at 400 °C for 10 h with a heating rate of 100° C/h followed by water quenching to promote the formation of dispersoids (Ref 15, 22). Then hot rolling was carried out on a lab-scale rolling mill with multiple passes at a temperature of ~400 °C with a reduction ratio of 85%. Before the mechanical tests, all hot-rolled sheets were heat-treated to the T6 temper involving solutionizing at 540 °C for 15 min, room-temperature water quenching, and artificial aging at 180 °C for 5 h. To study the thermal stabilities of rolled sheets, some of the T6-treated samples were further subjected to thermal exposure at 300 °C for 100 h referred to herein as T6A condition.

The tensile test samples were machined in the rolling direction according to ASTM standard E8/E8 M-13a with a rectangular cross-section of 3 × 6 mm and a length of 25 mm in the gauge area. The elevated-temperature tensile properties were measured at 300 °C using a Gleeble 3800 thermomechanical simulator at a strain rate of 10^{-3} s^{-1}, where the samples were preheated at a heating rate of 2 °C/s and held for 3 min to achieve a uniform temperature distribution before testing. The room-temperature tensile properties were measured using an Instron 8801 servo-hydraulic unit with a strain rate of 0.5 mm/min. For both room- and elevated-temperature properties, at least three samples were tested per condition and the average values were obtained. For reliable comparison of alloy properties, the statistical significance of the average values was examined using a t-test (Ref 25), and wherever they were compared indicating high/low differences in alloy properties, they were found satisfying 95% confidence interval criteria ($\alpha = 0.05$).

A transmission electron microscope (TEM, Jeol JEM-2100) was used to observe the nanoscale dispersoids and precipitates in detail. The preparation and observation of the TEM samples as well as the calculation of the volume fraction of dispersoids, V_v, were conducted as explained in the previous study (Ref 22). The number density of dispersoids, N_D, was calculated according to the following equation (Ref 23):

$$N_D = \frac{N}{A(\bar{D} + t)} \quad (1)$$

where N is the number of dispersoids in the TEM image, A is the area of the TEM image, $\bar{D}$ is the average equivalent diameter of dispersoids, and t is the TEM foil thickness in the imaged area. The number density of the precipitates, N_p, was calculated from the following equation (Ref 26, 27):

$$N_P = \frac{3N_{\parallel}}{A(t + \langle l \rangle)} \quad (2)$$

where $N_{\parallel}$ is the number of precipitate cross-sections in the imaged area and $\langle l \rangle$ is the average needle length, while A and t are as defined previously for Eq. (1). The factor 3 considers the three equivalent directions of $\langle 100 \rangle_{Al}$, where the needle precipitates grow isotropically.

In order to investigate the effect of the dispersoids on the precipitation of the MgSi precipitates, differential scanning calorimetry (DSC) analysis was conducted on as-quenched samples. DSC analysis could reveal the solid-state phase transformation reactions, which correspond the formation of MgSi precipitates during heating the as-quenched samples, simulating the aging treatment of the alloys. During testing, these reactions cause changes in the measured heat flow, which appear on the DSC curve (heat flow *vs*. temperature) as peaks referred to as exothermic peaks. The temperatures of these peaks make it possible to identify the precipitates formed based on their reported precipitation temperatures. In addition, the peak areas (enthalpies) are proportional to the amounts of the precipitates, and therefore, could be used to compare these amounts under different conditions. The test was conducted using a Mettler Toledo differential scanning calorimeter under a protective atmosphere of pure argon at a flow rate of 30 mL/min. The mass of the DSC sample was approximately 20 mg and the heating scans were recorded between 25 °C and 580 °C at a heating rate of 10 °C/min.

3. Results and discussion

3.1. Effect of thermomechanical processing on the dispersoids

After homogenization, no dispersoids could be found in the base A alloy due to the absence of TEs in this alloy. In contrast, a large number of dispersoids were formed in alloys B, E and F. The bright-field TEM images in Fig. 2a-c show the submicron dispersoids formed during homogenization in these alloys. The morphology of the dispersoids was mostly a mixture of plate-like and cubic morphologies,

consistent with reported morphologies of α-Al(MnFe)Si type dispersoids in literature (Ref 13, 14). The dispersoids in alloys B, E, and F were identified as α-Al(MnFe)Si, α-Al(MnFeCrV)Si and α-Al(MnFeMo)Si dispersoids, respectively, using the TEM-EDS analysis and the selected area diffraction pattern (SADP) (Ref 22).

The TEM images in Fig. 2d-f show the dispersoid microstructures of alloys B, E, and F in the T6A condition, namely after the entire thermomechanical process, including homogenization, hot rolling, and T6 heat treatment followed by thermal exposure at 300 ºC for 100 h. Generally, the morphology of all dispersoids was transformed from the plate-like and cubic ones exhibited in the as-homogenized condition (Fig. 2a-c) to a spherical morphology. In addition, the size of the dispersoids remarkably increased and their number density decreased. These features reveal the progressive coarsening of the dispersoids, which took place during hot rolling and the subsequent solutionizing, taking into consideration that the thermal exposure at 300 ºC for 100 h had almost no coarsening effect on the dispersoids (Ref 7, 13, 14).

The characteristics of the dispersoids in the T6A condition are listed in Table 2 in comparison with those in the as-homogenized condition (Ref 22). The volume fractions were almost similar in both conditions, but the equivalent diameters were larger and the number densities were lower in the T6A condition due to the coarsening occurred during hot rolling and solutionizing. When compared with the as-homogenized condition, the equivalent diameter was increased by 78, 40, and 15%, whereas the number density was decreased by 89, 74, and 50% in alloys B, E, and F, respectively. It is apparent that alloy B (Mn only) exhibited the most observable dispersoid coarsening, while alloy F (Mn and Mo) possessed the highest resistance to dispersoid coarsening. This reveals the beneficial effect of Cr, V, and Mo in decreasing the growth kinetics and the coarsening of dispersoids in alloys E and F through the substitution of these elements of low diffusivities (Ref 10) for Mn and Fe in α-Al(MnFe)Si dispersoids to form more thermally stable α-Al(MnFeCrV)Si and α-Al(MnFeMo)Si dispersoids, respectively.

3.2. Precipitate microstructure

The general precipitation sequence of Al-Mg-Si 6xxx alloys was reported to be: supersaturated solid solution (SSS) → Mg-Si atomic clusters → GP zones → β'' → β', U1, U2, B′ → β, Si, where the β'' phase is deemed as the main strengthening phase of these alloys (Ref 28, 29). The bright-field TEM images in Fig. 3 show the precipitate microstructures of the four hot-rolled alloys in the T6 condition. The microstructure of the base A alloy was dominated by a high number density of fine needle-like

precipitates lying on $\{200\}_{Al}$ planes with an average length of 28 nm and an average cross-sectional diameter of 2.5 nm (Fig. 3a). Based on previous studies (Ref 8, 30), precipitates of such size and morphology were identified as β'' precipitates. Faint cross-shaped streaks along $\langle 100 \rangle_{Al}$ directions also appeared in the corresponding SADP (see the inset in Fig. 3a) characterizing β'' precipitates (Ref 31, 32). On the other hand, the microstructures of the dispersoid-containing alloys (B, E, and F) consisted of a mixture of α- dispersoids and MgSi precipitates which were mostly β'' precipitates (Fig. 3b to d). Two additional features were also observed in the microstructures of these alloys: (i) the presence of relatively coarse MgSi precipitates nucleated at α-dispersoids (indicated by small black and white arrows), which were similarly observed in other dispersoid-containing 6082 alloys and identified as either β' or B′ precipitates (Ref 8, 33), and (ii) the presence of β'' precipitate free zones around α-dispersoids. It was reported that α-Al(MnFe)Si dispersoids increased the quench sensitivity of 6xxx Al-Mg-Si alloys, acting as preferential heterogeneous nucleation sites for β'/B′ precipitates during quenching (Ref 33-35). However, the high cooling rate of the water quenching used in this study (120 ºC/s) is not supposed to allow the heterogeneous precipitation during quenching, and therefore, these coarse β'/B′ precipitates most likely nucleated and grew on the pre-existing α-dispersoids during aging, as previously indicated by Rakhmonov *et al*. (Ref 8). The characteristics of β'' precipitates in all alloys were quantitatively analyzed, and the results are presented in Table 3. It is apparent that the base A alloy possessed the highest number density and the smallest size of β'' precipitates followed by alloy E. In contrast, both alloys B and F had remarkably lower number densities and larger sizes of β'' precipitates.

After thermal exposure at 300 ℃ for 100 h, the β'' phase formed in all four alloys in the T6 condition was completely transformed to the equilibrium β-Mg_2Si phase due to the instability of β'' phase at high temperatures (Ref 8). Thus, in the base A alloy, there were only coarse β-Mg_2Si and Si particles left (Fig. 4a), which have no strengthening effect in the aluminum matrix. On the other hand, in the dispersoid-containing alloys, the relatively fine dispersoids remained in the aluminum matrix beside these coarse β-Mg_2Si and Si particles, showing almost no further coarsening during the thermal exposure (Fig. 4b and c) with size and distribution comparable to those in the T6 condition (Fig. 3c and d).

To further reveal the effect of dispersoids on the precipitation of MgSi precipitates in the dispersoid-containing B, E, and F alloys in comparison with the base A alloy, DSC analysis was conducted on as-quenched samples and the resulting heating curves are shown in Fig. 5. The DSC curve of the base alloy exhibited six exothermic peaks, I, II, III, IV, V, and VI at 77, 204, 258, 293, 438, and 547 ºC, respectively. Based on previous DSC analyses of Al-Mg-Si 6xxx alloys (Ref 30, 36-38), these

peaks can be attributed to the formation of Mg-Si clusters, GP zones, β'' phase, β' and/or B′ phases, excess Si, and β-Mg_2Si phase, respectively. The DSC curve of alloy E showed the same peaks as that of alloy A, but the areas of peaks I, II, and III became relatively smaller. For the other two dispersoid-containing alloys (B and F), the exothermic peak I almost disappeared and both exothermic peaks II and III were overlapped with decreased peak areas compared with alloys A and E.

Based on the above DSC results, it seems that the clustering of Mg and Si atoms was reduced or supressed in the dispersoid-containing alloys (B, E, and F), which in turn decreased the precipitation of GP zones and β'' precipitates to different extents compared with the dispersoid-free base A alloy. It was reported that the annihilation of the quenched-in vacancies significantly affected the precipitation process in Al-Mg-Si 6xxx alloy by hindering the formation of Mg-Si clusters and consequently decreasing β'' precipitates (Ref 34). Prasad *et al*. (Ref 39) and Starke *et al*. (Ref 40) reported that the noncoherent interfaces between α-Al and Mn-bearing dispersoids could act as sinks for quenched-in vacancies. These findings could explain the decrease of the precipitation of Mg-Si clusters and β'' precipitates in the dispersoid-containing alloys, which was also confirmed by the lack of β'' precipitates in the vicinity of α-dispersoids (Fig. 3b to d). The formation enthalpies of β'' precipitates in all alloys are listed in Table 4, where the highest enthalpy was attained in the dispersoid-free base A alloy (4.64 J/g). Among the three dispersoid-containing alloys, alloy B exhibited the lowest enthalpy for β'' precipitates followed by alloys F and E (2.38, 2.83, and 3.52 J/g, respectively), which inversely correlated with the volume fractions of the dispersoids presented in these alloys (1.82%, 1.36%, and 1.06%, respectively, Table 2). This indicates that the amounts of β'' precipitates decreased with increasing the volume fraction of dispersoids, as the annihilation of quenched-in vacancies would increase with increasing the volume fraction of dispersoids. It was reported that Mg-Si clusters, GP zones, and β'' phase have the same Mg:Si atomic ratio (Ref 41, 41), and both Mg-Si clusters and GP zones serve as nucleation sites for the β'' precipitates (Ref 41-43). Thus, both alloys A and E containing abundant Mg-Si clusters (peak I, Fig. 5) had denser and finer β'' precipitates compared to alloys B and F, as confirmed by the TEM observation (Fig. 3) and the quantitative analysis of β'' phase (Table 3).

3.3. Room- and elevated-temperature tensile properties

Fig 6 shows the room-temperature tensile properties of the experimental alloys in the T6 condition, where the base A alloy exhibited yield strength (YS) and ultimate tensile strength (UTS) of 267 and 306 MPa, respectively. In comparison, the dispersoid-containing B alloy exhibited lower YS

and UTS of 244 and 290 MPa, whereas the other two dispersoid-containing E and F alloys showed more or less comparable YS and UTS of 255-260 and 300 MPa, respectively. It is apparent that the strengths of the T6-treated alloys at room temperature were controlled by the characteristics of both β'' precipitates and α-dispersoids in the alloys (Tables 2 and 3). The α-dispersoids may play a minor role in the overall strengthening of the alloys at room temperature depending on their size and number density. In alloy A, no dispersoids were formed, but the β'' precipitates attained their highest amount and smallest size (Fig. 5 and Table 3), resulting in high YS and UTS. On the other hand, alloy B had the lowest number density and the largest size for both β'' precipitates and α-dispersoids, and therefore exhibited lower strengths. Using the t-test for two-average comparison (Ref 25), it was confirmed that the differences in the strengths between alloys A and B were statistically significant ($\alpha < 0.05$). In alloys E and F, the characteristics of β'' precipitates and α-dispersoids were better relative to alloy B. The relatively higher number densities and smaller sizes of the dispersoids in alloys E and F (Table 2) enhanced the dispersion strengthening and, consequently, compensated for the decrease of the precipitation strengthening of β'' precipitates to some extent; thus both alloys had strengths nearly comparable to those of alloy A. The elongation to break (El), which was generally affected by the primary intermetallic phases, MgSi precipitates, and α-dispersoids, ranged between 10.1 and 13.7%.

Fig 7 shows the elevated-temperature tensile properties of the experimental alloys in the T6 condition and after thermal exposure at 300 ºC for 100 h, namely the T6A condition. In the T6 condition (no thermal exposure, Fig. 7a), the alloys showed YSs of 95-100 MPa and UTSs of 99-108 MPa, which were lower than those attained at room temperature (Fig. 6) by 61-64% and 64-68%, respectively, due to the softening of the aluminum matrix during testing at 300 ºC. It seems that the strengths of the experimental alloys in this condition more or less maintained the trend taken when testing at room temperature (Fig. 6) but with lower values. This implies that the precipitation hardening might still play its role in the alloys as occurred at room temperature but with the less effective strengthening β'/B' phase that was evolved from the β'' phase during the tensile test at 300 ºC and not yet transformed to the equilibrium, non-strengthening β-Mg_2Si phase, as this test lasted only a few minutes. Yuan *et al*. (Ref 44) found that semi-coherent β' and B' precipitates reaching 70 nm in length were still present in an aged Al-Mg-Si alloy after 50 h of thermal-resistant treatment at 180 ºC.

After 300ºC/100h thermal exposure (T6A condition, Fig. 7b), the YS and UTS of all four alloys were significantly decreased, because both β'' and β'/B' phases were completely transformed to the equilibrium β-Mg_2Si phase (Fig. 4), which had no strengthening effect on the alloys. The YS and UTS

of the dispersoid-free base A alloy dropped to 31 and 43 MPa, respectively, while the YSs and UTSs of the dispersoid-containing B, E, and F alloys became much higher, ranging from 53 to 70 MPa and 61 to 76 MPa, respectively. Accordingly, the improvements of the elevated-temperature YS and UTS of the dispersoid-containing alloys were 71-126% and 42-77%, respectively, which can be attributed to the dispersion strengthening of the thermally stable α-dispersoids that showed almost no coarsening during thermal exposure (Fig. 4). The highest strengths were exhibited by alloy F followed by alloys E and B, which is consistent with the size and number density of the dispersoids contained in these alloys after undergoing the whole thermomechanical process (Table 2, T6A). Using the t-test (Ref 25), the comparisons of the alloy strengths between the four alloys were generally found statistically significant ($\alpha << 0.05$). Generally, the ductility is not of primary concern when evaluating the elevated-temperature mechanical performance of the alloys, as the elongation reached outstanding values of 28-37% in the T6 condition (Fig. 7a) and even 41-74% in the T6A condition (Fig. 7b).

The evaluation of the tensile properties of the hot-rolled sheets indicates that the dispersoid-free A alloy attained room-temperature tensile properties exceeding those specified for commercial 6082-T6 sheets (YS, UTS, and El of 267 MPa, 306 MPa, and 12.8% *vs*. 250-255 MPa, 290-295 MPa, and 8-10% (Ref 45-47), respectively). However, the elevated-temperature performance of alloy A was quite poor (YS and UTS of 31 and 43 MPa, respectively), which limits its use in thermal- and fire-resistant structures. On the other hand, although the precipitation hardening was decreased in the dispersoid-containing B, E, and F alloys, the room-temperature tensile properties of both E and F alloys (YS = 255-260 MPa, UTS = 300 MPa, and El = 10.1-13.7%) were still high enough to meet the required room-temperature tensile properties of these commercial 6082-T6 sheets. Most interestingly, these two alloys also exhibited remarkably high elevated-temperature YS and UTS after thermal exposure, which exceeded those of the dispersoid-free A alloy by 1.9-2.3 times and 1.6-1.8 times, respectively. Therefore, 6082 alloys microalloyed with Cr, V, and Mo in combination with Mn could offer excellent combinations of room- and elevated-temperature mechanical properties, which in turn enables the use of the hot-rolled 6082 alloys in more critical applications.

4. Conclusions

The microstructure and room/elevated-temperature tensile properties of hot-rolled 6082 alloys were studied. In addition to a benchmark Mn-free alloy with no dispersoids, three other alloys containing Mn individually and in combinations with Cr + V or Mo were included, where a number of α-Al(MnFe)Si,

α-Al(MnFeCrV)Si, and α-Al(MnFeMo)Si dispersoids were formed, respectively. From the results obtained, the following conclusions can be drawn:

1. The α-Al(MnFeCrV)Si, and α-Al(MnFeMo)Si dispersoids exhibited low coarsening compared with α-Al(MnFe)Si dispersoids due to the lower diffusivity of Cr, V, and Mo, thereby possessing higher number densities and smaller sizes after thermomechanical processing and thermal exposure.
2. The presence of α-dispersoids hindered the formation of Mg-Si clusters, which decreased the precipitation of β''-MgSi phase and consequently the room-temperature strengths, particularly in the alloy containing α-Al(MnFe)Si dispersoids. The precipitation of β''-MgSi phase was proportionally decreased with increasing the volume fraction of the dispersoids.
3. After thermal exposure at 300 ºC, all β'' and β' precipitates were transformed to equilibrium, non-strengthening β-Mg_2Si phase particles. On the other hand, the α-dispersoids remained thermally stable and became the predominant strengthening phase, increasing the YS and UTS at 300 ºC by 71-126% and 42-77%, respectively, relative to the base alloy without dispersoids.
4. Among the three dispersoid-containing alloys studied, the alloy containing Mn and Mo exhibited the highest YS of 70 MPa and UTS of 76 MPa at 300 ºC, providing the best combination of room- and elevated-temperature tensile properties, which could allow the use of the hot-rolled 6082 alloys in more critical applications.

Acknowledgments

The authors would like to acknowledge the financial support of the Natural Sciences and Engineering Research Council of Canada (NSERC) under the Grant No. CRDPJ 514651-17 through the Research Chair in the Metallurgy of Aluminum Transformation at University of Quebec at Chicoutimi.

References

1. Y. Birol, The Effect of Processing and Mn Content on the T5 and T6 Properties of AA6082 Profiles, *J. Mater. Process. Technol.*, 2006, **173**(1), p 84–91
2. V. Kumar and D. Kumar, Investigation of Tensile Behaviour of Cryorolled and Room Temperature Rolled 6082 Al Alloy, *Mater. Sci. Eng. A*, 2017, **691**, p 211–217
3. Y. Liu, H. Liu, and Z. Chen, Post-Fire Mechanical Properties of Aluminum Alloy 6082-T6, *Constr. Build. Mater.*, 2019, **196**, p 256–266
4. E.J. Fogle, B.Y. Lattimer, S. Feih, E. Kandare, A.P. Mouritz, and S.W. Case, Compression Load Failure of Aluminum Plates due to Fire, *Eng. Struct.*, 2012, **34**, p 155–162
5. Z. Chen, J. Lu, H. Liu and X. Liao, Experimental Investigation on the Post-Fire Mechanical Properties of Structural Aluminum Alloys 6061-T6 and 7075-T73, *Thin-Walled Struct*., 2016, **106**, p 187–200
6. J. Rakhmonov, K. Liu, P. Rometsch, N. Parson and X.-G. Chen, Improving the Mechanical Response of Al–Mg–Si 6082 Structural Alloys during High-Temperature Exposure through Dispersoid Strengthening, *Materials*, 2020, **13**(22), 5295
7. K. Ma, E.M. Elgallad, Z.X. Chen, B.L. Xiao and X.-G. Chen, Improving the Elevated-Temperature Mechanical Properties of AA3004 Hot-Rolled Sheets by Microalloying with Mo and Optimizing the Process Route, *J. Mater. Res. Technol*., 2022, **19**, p 4489–4503
8. J. Rakhmonov, K. Liu, P. Rometsch, N. Parson and X.-G. Chen, Effects of Al(MnFe)Si Dispersoids with Different Sizes and Number Densities on Microstructure and Ambient/Elevated-Temperature Mechanical Properties of Extruded Al-Mg-Si AA6082 Alloys with Varying Mn Content, *J. Alloys Compd*., 2021, **861**, 157937
9. W. Yuan, Z. Liang, C. Zhang, and L. Wei, Effects of La Addition on the Mechanical Properties and Thermal-Resistant Properties of Al–Mg–Si–Zr Alloys Based on AA6201, *Mater. Des*., 2012, **34**, p 788–792
10. Keith E. Knipling, David C. Dunand, and David N. Seidman, Criteria for Developing Castable, Creep-Resistant Aluminum-Based Alloys - A Review, *Int. J. Mater. Res*., 2006, **97**(3), p 246–265
11. Y.J. Li and L. Arnberg, Quantitative Study on the Precipitation Behavior of Dispersoids in DC-Cast AA3003 Alloy during Heating and Homogenization, *Acta Mater*., 2003, **51**(12), p 3415–3428

12. A.Y. Algendy, K. Liu, and X.-G. Chen, Evolution of Dispersoids during Multistep Heat Treatments and their Effect on Rolling Performance in an Al-5% Mg-0.8% Mn Alloy, *Mater. Charact.*, 2021, **181**, 111487
13. K. Liu and X.-G. Chen, Development of Al–Mn–Mg 3004 Alloy for Applications at Elevated Temperature via Dispersoid Strengthening, *Mater. Des*., 2015, **84**, p 340–350
14. Z. Li, Z. Zhang, and X.-G. Chen, Microstructure, Elevated-Temperature Mechanical Properties and Creep Resistance of Dispersoid-Strengthened Al-Mn-Mg 3xxx Alloys with Varying Mg and Si Contents, *Mater. Sci. Eng. A*, 2017, **708**, p 383–394
15. C. Li, K. Liu, and X.-G. Chen, Improvement of Elevated-Temperature Strength and Recrystallization Resistance via Mn-Containing Dispersoid Strengthening in Al-Mg-Si 6082 Alloys, *J. Mater. Sci. Technol*., 2020, **39**, p 135–143
16. J. Rakhmonov, K. Liu, P. Rometsch, N. Parson and X.-G. Chen, Enhanced Elevated-Temperature Strength and Creep Resistance of Dispersion-Strengthened Al-Mg-Si-Mn AA6082 Alloys through Modified Processing Route, *Materials*, 2021, **14**(19), 5489
17. H.-W. Huang and B.-L. Ou, Evolution of Precipitation during Different Homogenization Treatments in a 3003 Aluminum Alloy, *Mater. Des*., 2009, **30**(7), p 2685–2692
18. Astrid Marie F. Muggerud, Eva Anne Mørtsell, Yanjun Li, and Randi Holmestad, Dispersoid Strengthening in AA3xxx Alloys with Varying Mn and Si Content during Annealing at Low Temperatures, *Mater. Sci. Eng. A*, 2013, **567**, p 21–28
19. Y.J. Li, A.M.F. Muggerud, A. Olsen, and T. Furu, Precipitation of Partially Coherent α-Al(Mn,Fe)Si Dispersoids and their Strengthening Effect in AA 3003 Alloy, *Acta Mater*., 2012, **60**, p 1004–1014
20. X. Qian, N. Parson, and X.-G. Chen, Effects of Mn Addition and Related Mn-Containing Dispersoids on the Hot Deformation Behavior of 6082 Aluminum Alloys, *Mater. Sci. Eng. A*, 2019, **764**, 138253
21. K. Liu, H. Ma, and X.-G. Chen, Improving the Elevated-Temperature Properties by Two-Step Heat Treatments in Al-Mn-Mg 3004 Alloys, Metall. Mater. Trans. B, 2018, **49**, p 1588-1596
22. E.M. Elgallad, K. Liu, Z. Zhang and X.-G. Chen, Effect of Transition Elements on Dispersoid Formation and Elevated-Temperature Mechanical Properties in 6082 Aluminum Alloy, *Philos. Mag.*, 2021, **101**(1), p 96–116

23. F. Qian, S. Jin, G. Sha and Y. Li, Enhanced Dispersoid Precipitation and Dispersion Strengthening in An Al Alloy by Microalloying with Cd, *Acta Mater*., 2018, **157**, p 114–125
24. K. Liu, H. Ma, and X.-G. Chen, Enhanced Elevated-Temperature Properties via Mo Addition In Al-Mn-Mg 3004 Alloy, *J. Alloys Compd*., 2017, 694, p 354–365
25. The t tests: Difference between means of two samples. https://www.bmj.com/about-bmj/resources-readers/publications/statistics-square-one/7-t-tests (accessed April 19, 2023).
26. J.K. Sunde, Ø. Paulsen, S. Wenner and R. Holmestad, Precipitate Statistics in an Al-Mg-Si-Cu Alloy from Scanning Precession Electron Diffraction Data, *J. Phys.: Conf. Ser.*, 2017, **902**, 012022
27. S.J. Andersen, Quantification of the Mg_2Si β″ and β′ Phases in AlMgSi Alloys by Transmission Electron Microscopy, *Metall. Mater. Trans. A*, 1995, **26**, p 1931–1937
28. S.J. Andersen, C.D. Marioara, R. Vissers, A. Frøseth and H.W. Zandbergen, The Structural Relation between Precipitates in Al–Mg–Si Alloys, the Al-Matrix and Diamond Silicon, with Emphasis on the Trigonal Phase U1-$MgAl_2Si_2$, *Mater. Sci. Eng. A*, 2007, **444**(1-2), p 157–169
29. M. Yang, H. Chen, A. Orekhov, Q. Lu, X. Lan, K. Li, S. Zhang, M. Song, Y. Kong, D. Schryvers and Y. Du, Quantified Contribution of β" and β' Precipitates to the Strengthening of an Aged Al–Mg–Si Alloy, *Mater. Sci. Eng. A*, 2020, **774**, 138776
30. G.A. Edwards, K. Stiller, G.L. Dunlop and M.J. Couper, The Precipitation Sequence in Al-Mg-Si Alloys, *Acta Mater*., 1998, **46**(11), p 3893–3904
31. W. Yang, M. Wang, R. Zhang, Q. Zhang and X. Sheng, The Diffraction Patterns from β" Precipitates in 12 Orientations in Al–Mg–Si Alloy, *Scr. Mater*., 2010, **62**(9), p 705–708
32. R.S. Yassar, D.P. Field and H. Weiland, Transmission Electron Microscopy and Differential Scanning Calorimetry Studies on The Precipitation Sequence in An Al–Mg–Si Alloy: AA6022, *J. Mater. Res.*, 2005, **20**, p 2705–2711
33. B. Milkereit and M.J. Starink, Quench Sensitivity of Al–Mg–Si Alloys: A Model for Linear Cooling and Strengthening, *Mater. Des.*, 2015, **76**, p 117–129
34. K. Strobel, M.A. Easton, M.D.H. Lay, P.A. Rometsch, S. Zhu, L. Sweet, N.C. Parson and A.J. Hill, Quench Sensitivity in a Dispersoid-Containing Al-Mg-Si Alloy, *Metall. Mater. Trans. A*, 2019, **50**, p 1957–1969
35. B. Milkereit, M.J. Starink, P.A. Rometsch, C. Schick and O. Kessler, Review of the Quench Sensitivity of Aluminium Alloys: Analysis of the Kinetics and Nature of Quench-Induced Precipitation, *Materials*, 2019, **12**(24), 4083

36. I. Dutta and S.M. Allen, A Calorimetric Study of Precipitation in Commercial Aluminium Alloy 6061, *J. Mater. Sci. Lett.*, 1991, **10**, p 323–326
37. Y. Birol, The Effect of Sample Preparation on the DSC Analysis of 6061 Alloy, *J. Mater. Sci.,* 2005, **40**, p 6357–6361
38. L. Zhen, W.D. Fei, S.B. Kang and H.W. Kim, Precipitation Behaviour of Al–Mg–Si Alloys with High Silicon Content, *J. Mater. Sci.,* 1997, **32**, p 1895–1902
39. K.S. Prasad, A.A. Gokhale, A.K. Mukhopadhyay, D. Banerjee and D.B. Goel, On the Formation of Faceted Al_3Zr (β') Precipitates in Al-Li-Cu-Mg-Zr Alloys, *Acta Mater.*, 1999, **47**(8), p 2581–2592
40. E.A. Starke, T.H. Sanders and I.G. Palmer, New Approaches to Alloy Development in the Al-Li System, *JOM*, 1981, **33**, p 24–33
41. S. Zhu, H.-C. Shih, X. Cui, C.-Y. Yu and S.P. Ringer, Design of Solute Clustering during Thermomechanical Processing of AA6016 Al–Mg–Si Alloy, *Acta Mater*., 2021, **203**, 116455
42. M. Murayama and K. Hono, Pre-Precipitate Clusters and Precipitation Processes in Al–Mg–Si Alloys, *Acta Mater.*, 1999, **47**(5), p 1537–1548
43. Y. Zheng, B. Luo, Z. Bai and C. He, Evolution of the Initial Precipitation and Strengthening Mechanism of Al-Mg-Si Alloys, *JOM*, 2019, **71**, p 4737–4745
44. W. Yuan and Z. Liang, Effect of Zr Addition on Properties of Al–Mg–Si Aluminum Alloy used for all Aluminum Alloy Conductor, *Mater. Des.*, 2011, **32**(8-9), p 4195–4200
45. Aircraft Materials. https://www.aircraftmaterials.com/data/aluminium/6082.html (accessed December 30, 2022).
46. Nedal Aluminium. https://www.nedal.com/wp-content/uploads/2016/11/Nedal-alloy-Datasheet-EN-AW-6082.pdf (accessed December 30, 2022).
47. MatWeb. https://www.matweb.com/search/QuickText.aspx?SearchText=6082 (accessed December 30, 2022).

Figure captions

Fig. 1. Thermomechanical processing route of 6082 alloy sheets. WQ and AC refer to water quenching and air-cooling, respectively.

Fig. 2. Bright-field TEM images showing the dispersoid microstructures of alloys B (a, d), E (b, e) and F (c, f) in the as-homogenized (a, b, c) and T6A (d, e, f) conditions.

Fig. 3. Bright-field TEM images showing the precipitate microstructures in the T6 condition: (a) the base A alloy, (b) alloy B, (c) alloy E, and (d) alloy F.

Fig. 4. Bright-field TEM images showing microstructures after thermal exposure at 300 ℃ for 100 h: (a) coarse β-Mg_2Si and Si particles in the base A alloy, (b, c) relatively fine dispersoids beside coarse β-Mg_2Si and Si particles in alloys E and F, respectively.

Fig. 5. DSC heating curves of the four experimental alloys in the as-quenched condition.

Fig. 6. Room-temperature tensile properties of 6082 alloys in the T6 condition.

Fig. 7. Tensile properties of 6082 alloys at 300 ºC in (a) T6 and (b) T6A conditions.

Tables

Table 1. Chemical compositions of the experimental 6082 alloys

Alloys	Elements (wt%)							
	Si	Fe	Mg	Mn	Cr	V	Mo	Al
A (base)	0.77	0.28	1.18	0.00	0.00	0.00	0.00	Bal.
B	0.82	0.29	1.16	**1.04**	0.00	0.00	0.00	Bal.
E	0.78	0.32	1.22	**1.05**	**0.22**	**0.25**	0.00	Bal.
F	0.77	0.31	1.16	**1.01**	0.00	0.00	**0.30**	Bal.

Table 2. Characteristics of the dispersoids in the as-homogenized and T6A conditions

Condition	As-homogenized (Ref 16)			T6A		
Alloy	B	E	F	B	E	F
Equivalent diameter ($\overline{D}$), nm	43.2 ± 3.3	30.4 ± 2.8	40.5 ± 2.2	76.8 ± 2.2	42.6 ± 3.0	46.4 ± 1.5
Volume fraction (V_v), %	1.85 ± 0.32	1.07 ± 0.26	1.24 ± 0.15	1.82 ± 0.40	1.06 ± 0.23	1.36 ± 0.19
Number density (N_D), μm^{-3}	952.6 ± 91.6	811.5 ± 57.8	615.4 ± 65.6	109.1 ± 15.6	214.7 ± 25.2	308.2 ± 30.0

Table 3. Characteristics of β'' phase in the experimental 6082 alloys

Alloy	A	B	E	F
Number density (N_p), 10^3 μm^{-3}	38.5 ± 0.4	4.8 ± 0.8	17.2 ± 1.0	6.0 ± 0.3
Average length (l), nm	28.1 ± 6.6	60.4 ± 7.2	30.6 ± 0.4	54.8 ± 5.1

Table 4. Formation enthalpies of β'' phase in the experimental 6082 alloys (peak III, Fig. 5)

Alloy	A	B	E	F
Enthalpy (J/g)	4.64	2.38	3.52	2.83

Figures

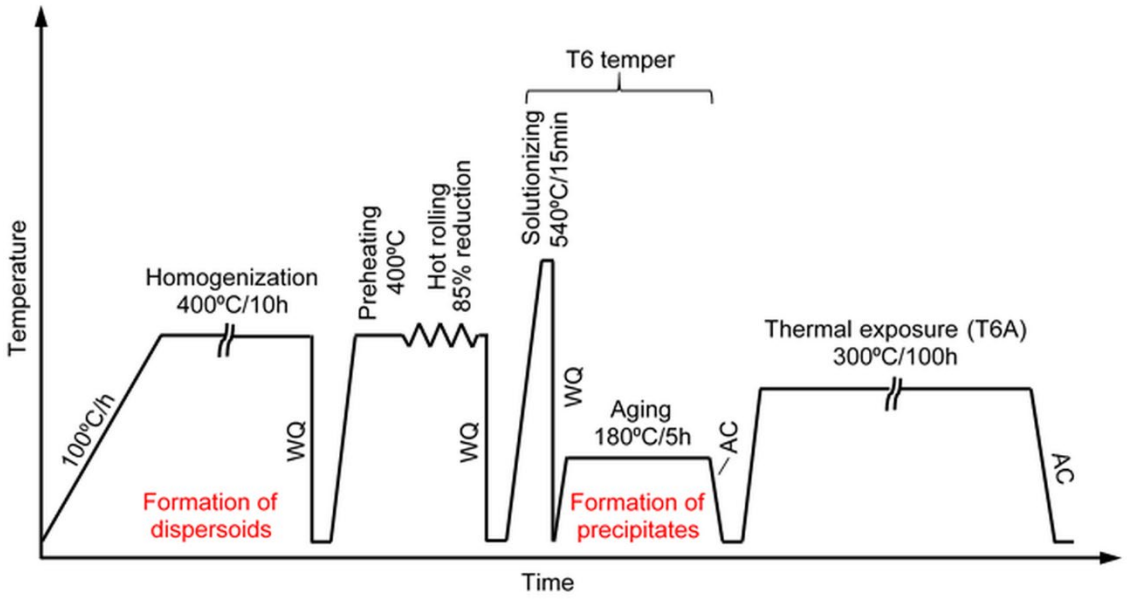

Fig. 1. Thermomechanical processing route of 6082 alloy sheets. WQ and AC refer to water quenching and air-cooling, respectively.

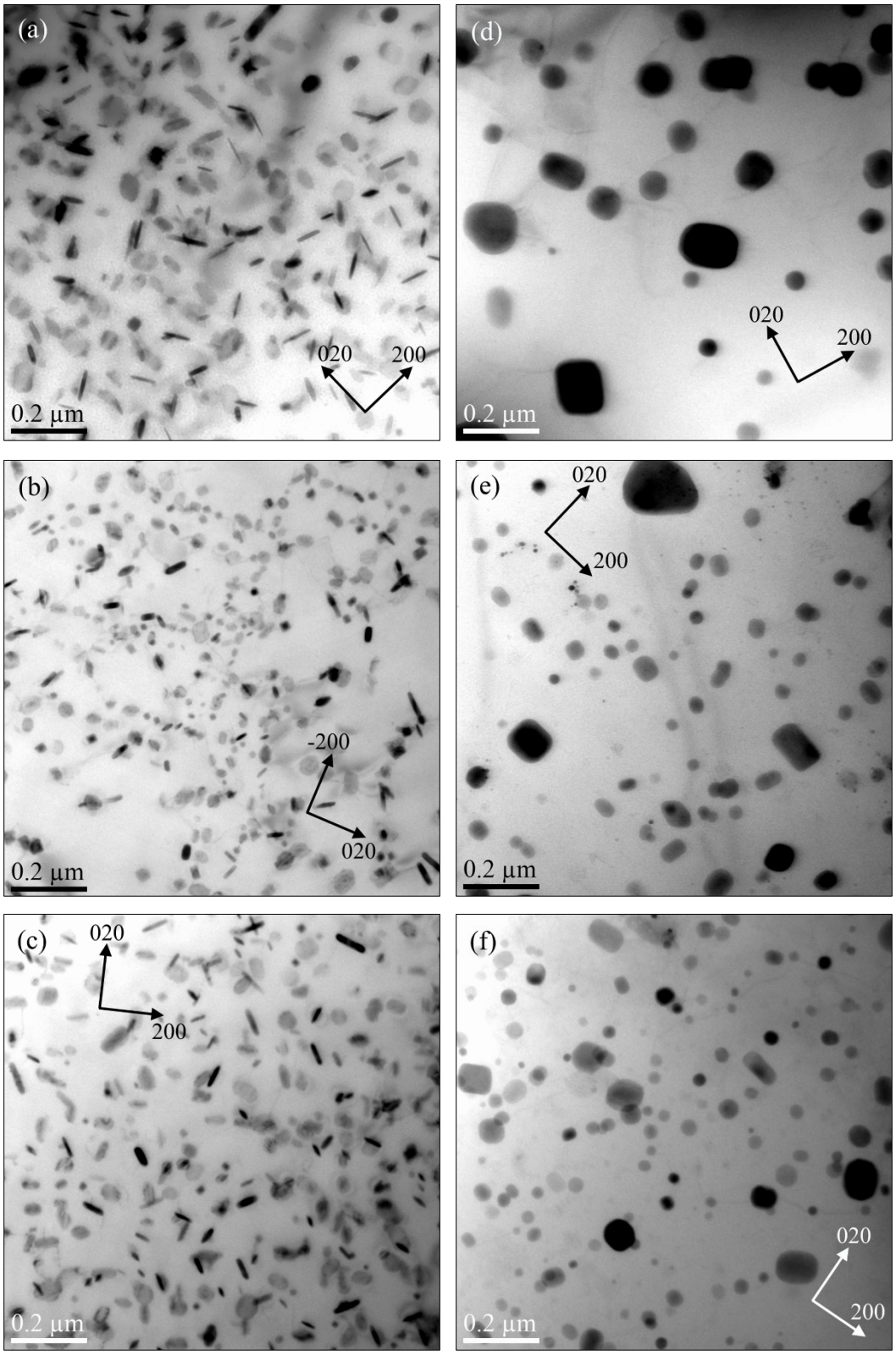
(a)
020
200
0.2 µm
(d)
020
200
0.2 µm
(b)
-200
020
0.2 µm
(e)
020
200
0.2 µm
(c)
020
200
0.2 µm
(f)
020
200
0.2 µm

Fig. 2. Bright-field TEM images showing the dispersoid microstructures of alloys B (a, d), E (b, e) and F (c, f) in the as-homogenized (a, b, c) and T6A (d, e, f) conditions.

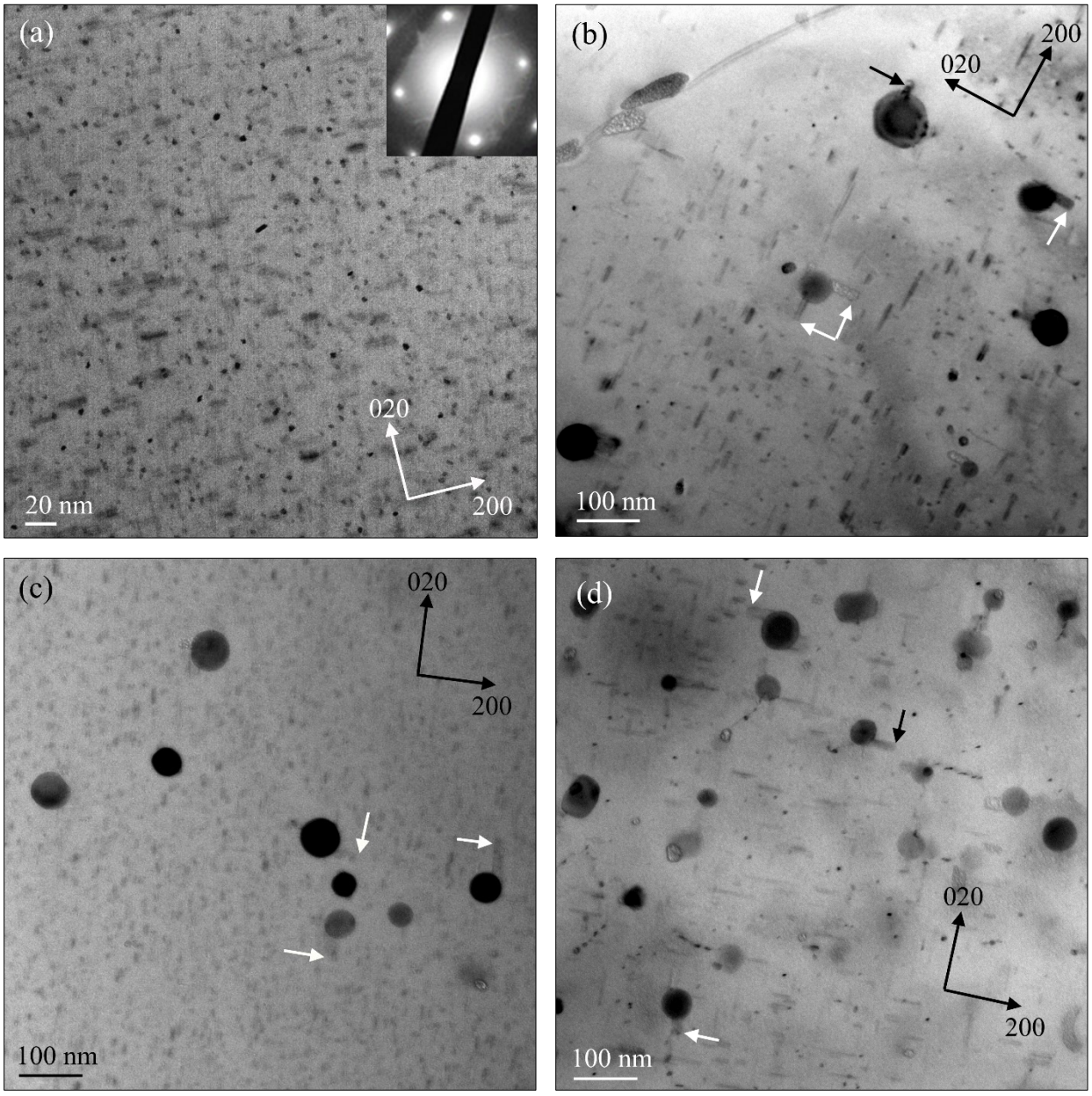

Fig. 3. Bright-field TEM images showing the precipitate microstructures in the T6 condition: (a) the base A alloy, (b) alloy B, (c) alloy E, and (d) alloy F.

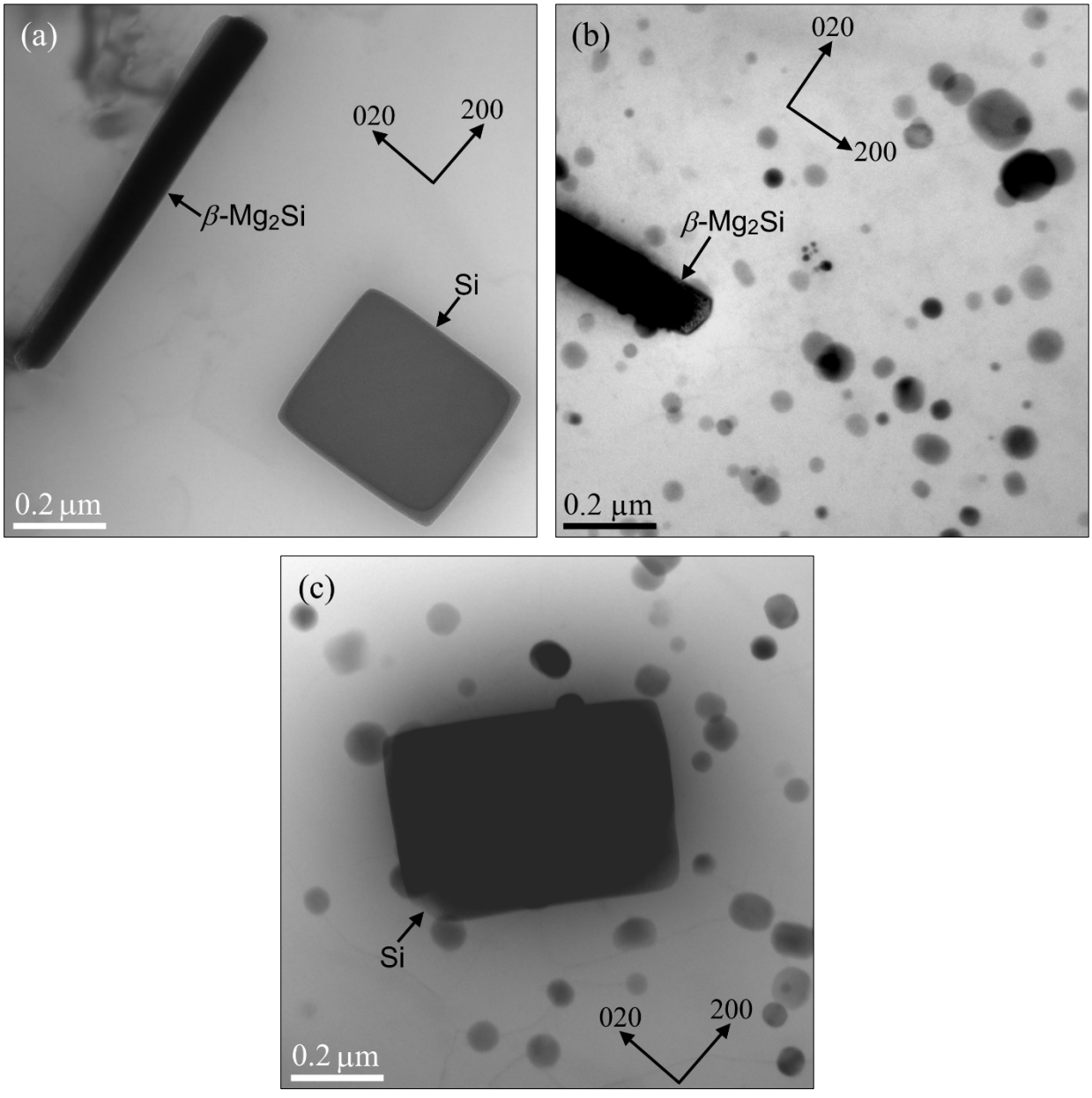

Fig. 4. Bright-field TEM images showing microstructures after thermal exposure at 300 ℃ for 100 h: (a) coarse β-Mg_2Si and Si particles in the base A alloy, (b, c) relatively fine dispersoids beside coarse β-Mg_2Si and Si particles in alloys E and F, respectively.

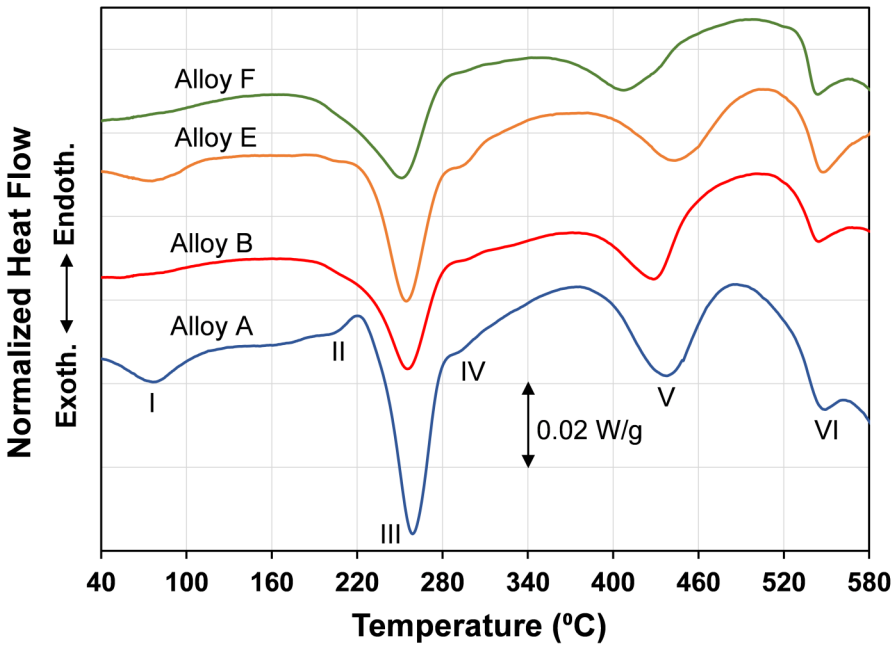

Fig. 5. DSC heating curves of the four experimental alloys in the as-quenched condition.

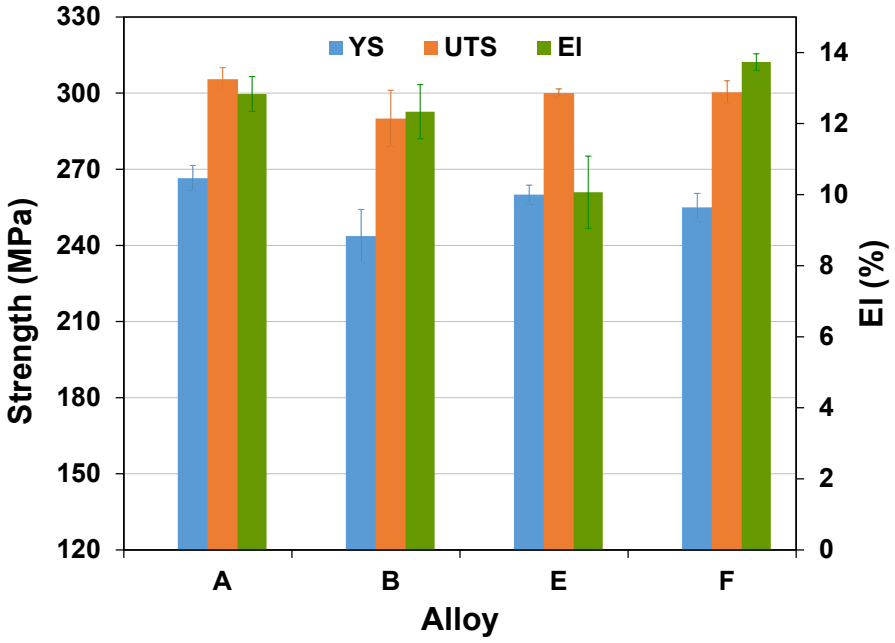

Fig. 6. Room-temperature tensile properties of 6082 alloys in the T6 condition.

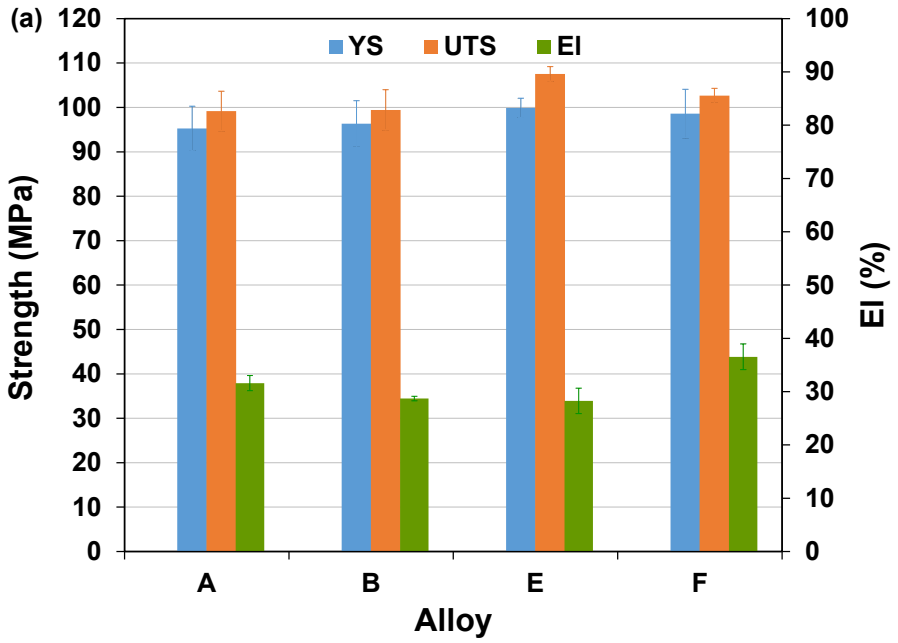

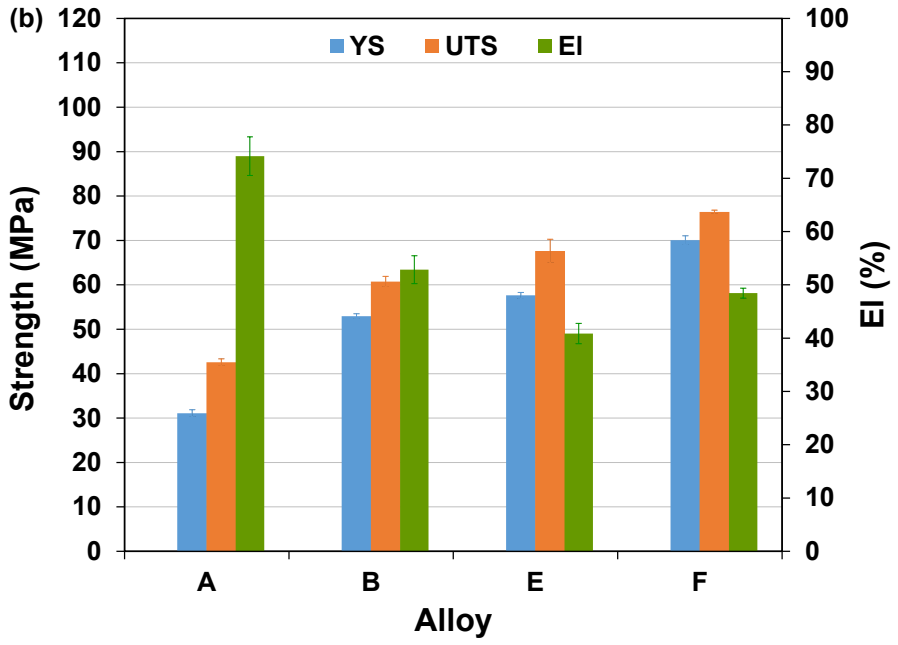

Fig. 7. Tensile properties of 6082 alloys at 300 ºC in (a) T6 and (b) T6A conditions.